Acta Materialia 220 (2021) 117344

Contents lists available at ScienceDirect

Acta Materialia

journal homepage: www.elsevier.com/locate/actamat

Full length article

Towards pressureless sintering of nanocrystalline tungsten

Xingyu Li[a], Lin Zhang[a,*], Yanhao Dong[b,*], Mingli Qin[a], Zichen Wei[a], Zhongyou Que[a], Junjun Yang[a], Xuanhui Qu[a], Ju Li[b,c,*]

[a] Beijing Advanced Innovation Center for Materials Genome Engineering, Institute for Advanced Materials and Technology, University of Science and Technology Beijing, Beijing 100083, China
[b] Department of Nuclear Science and Engineering, Massachusetts Institute of Technology, Cambridge, MA 02139, USA
[c] Department of Materials Science and Engineering, Massachusetts Institute of Technology, Cambridge, MA, 02139, USA

ARTICLE INFO

Article history:
Received 1 June 2021
Revised 8 August 2021
Accepted 19 September 2021
Available online 23 September 2021

Keywords:
Powder metallurgy
Porosity
Two-step sintering
Grain growth
Mechanical properties

ABSTRACT

The challenge of sintering ultrafine-grained tungsten to >99% density and towards nanocrystallinity is hereby addressed by optimized pressureless two-step sintering. It successfully produced tungsten samples with 99.3% theoretical density and 290 nm average grain size, with a uniform grain structure, good grain boundary cohesion, and 7.8 GPa hardness that is the highest in all pressurelessly sintered tungsten. The critical role of initial powders and the resultant green bodies was noted, which greatly affects later-on sintering kinetics and microstructural uniformity. Several key questions concerning two-step sintering of metallic tungsten were addressed, including the selection of the first- and second-step sintering temperatures, the thermodynamically required critical density to start the second-step sintering, and grain growth kinetics during sintering. The lessons learned here should be directly transferable to other refractory metals and their alloys and would help address the ultimate task of pressureless sintering of bulk nanocrystalline refractory metals/alloys.

1. Introduction

Fine-grained tungsten (W) is of great interest both as a model system of an elementary metal with the highest melting point and being useful in many technologies, including fusion energy, aerospace, microelectronics and other applications under extreme environments [1,2]. Refining the as-sintered microstructure to ultrafine-grained and ultimately to nanocrystalline grain size and with low porosity and high spatial uniformity is much desired in terms of improved properties and reliability [3–5], including ductility [6]. While dopant-enabled activated sintering [7–11] and field-assisted sintering [12–17] are known to help, high purity, high-temperature properties and flexibility in the sample size and geometry are preferred in certain applications, e.g., as sputtering targets and in additive manufacturing. Yet it is very challenging as solid-state pressureless sintering of pure W typically requires high temperature above 1500 °C, and concurrent grain growth under the same capillarity driving force as sintering can rapidly coarsen the grain size. This is especially problematic for nanopowders (which is required to produce ultrafine-grained and nanocrystalline W, since the size can only grow in sintering), because: (i) they generally have lower packing density in the green body than the coarse powders, (ii) their nano-size benefit is quickly exhausted, and (iii) the large capillarity force can drive fast grain boundary migration, which induces pore-grain boundary separation, creates in-grain porosity that can hardly be removed, and bifurcates the microstructure with heterogeneous and localized sintering. Therefore, sintering of nanopowders should be conducted at low temperatures, and the kinetics of sintering (porosity reduction) and grain growth (grain size increase) need to be decoupled as much as possible.

Pressureless two-step sintering is an effective approach to solve the above problems [18–20]. In a typical two-step sintering experiment, the compacted green body is firstly heated up to a higher temperature T_1 without holding to reach a relative density ρ>70-80%, which shrinks the relative size of the pores and pore channels (with respect to the grain size) to thermodynamically unstable values (thus sinterable). It is then cooled down to a lower temperature T_2 (typically 100-200 °C lower than T_1) and held at T_2 until nearly full density is reached. The second-step sintering at T_2 is able to allow densification while suppressing grain growth. Completely frozen grain size can be achieved with the best practice. Since the first demonstration in Y_2O_3, two-step sintering has been successfully applied to many ceramic systems [18–27], which not only refines the grain size of pressureless sintered samples to ~30 nm but also homogenizes the microstructure with better-

* Corresponding authors.
E-mail addresses: zlin@ustb.edu.cn (L. Zhang), dongyh@mit.edu (Y. Dong), liju@mit.edu (J. Li).

https://doi.org/10.1016/j.actamat.2021.117344
1359-6454/

than-Lifshitz-Slyozov-Wagner-Hillert grain-size uniformity and improved properties and reliabilities [3,5]. Despite the apparent relevance to powder metallurgy, this method has not been widely employed in metallic systems. The first attempt on body-center-cubic (BCC) refractory metals was made by us recently [4], which produces ultrafine-grained pure W with ρ>98% and average grain size G_{avg}≈700 nm. While it presents one of the best pressureless sintering practices of W, there are several remaining problems to be answered:

(1) The two-step sintering of W was conducted in pure H_2 atmosphere, and a holding time of 1 h at T_1 was used to remove trace oxygen impurity, which was thought to be critical for full densification and good grain boundary cohesion. But this T_1 holding would unavoidably coarsen the microstructure. Is it possible to completely eliminate such T_1 holding and still sinter W to full density with good mechanical properties?

(2) A critical density ρ_c=89% (obtained with the first-step sintering at T_1=1300 °C for 1 h) was found necessary to allow for full densification at T_2. Such a density is much higher than what is required for ceramic systems (e.g., ρ_c≈73% for $BaTiO_3$ [20], ≈75% for Y_2O_3 [18,19], ≈76% for $Ni_{0.2}Cu_{0.2}Zn_{0.6}Fe_2O_4$ [20], and ≈83% for Al_2O_3 [21,22]), despite that W has a relatively isotropic crystal structure. Is it possible to start the second-step sintering with lower ρ_c?

(3) A minimum T_2=1200 °C was found necessary for full densification, raising ρ≈89% to ≈98% in 10 h. However, it also increases G_{avg} from 530 nm after the first-step sintering to 700 nm in the fully densified sample. Is it possible to further lower T_2 and suppress grain growth in the second-step sintering?

(4) Even though we started with W nanopowders with a median particle size around 50 nm, the two-step sintered samples manifested G_{avg}≈700 nm in the end. This 14-fold coarsening is much larger than <2 for $BaTiO_3$-based ceramics [20] and 6-10 for Al_2O_3 [21,22]. Is it possible to achieve a lower coarsening ratio from the initial powder size to the final grain size?

In the present work, we seek to answer the above questions on two-step sintering of W. We found much room for improvement, and the critical role of the initial powders is revealed, which later translated to better sintering kinetics and spatial uniformity. By using modified powders, eliminating T_1 holding and optimizing the sintering schedule, we were able to two-step sinter W to ρ=99.3% and G_{avg}=290 nm, with 7.8 GPa hardness that is highest in all pressureless sintered W. This represents a major advance where ~6-fold coarsening is realized from powders to sintered pieces. To the end, we discussed other additive approaches to further improve sintering, which could pave the way toward pressureless sintering of dense nanocrystalline W (i.e., with G_{avg}<100 nm).

2. Experimental procedures

W nanopowders (purity: 99.9%) were prepared by a solution-combustion method followed by reduction in pure hydrogen, using ammonium metatungstate hydrate $(NH_4)_6H_2W_{12}O_{40}{\bullet}xH_2O$ as the precursor [28]. The obtained W powders were either directly used (termed as raw powders) or sieved to remove the large particles [29] (termed as sieved powders). The sieving process was conducted by dispersing the raw powders in anhydrous ethanol and centrifuging at 3000 rpm. The powders were uniaxially pressed at 750 MPa to prepare green compacts with a diameter of 10 mm and a thickness of ~1 mm. Sintering experiments were conducted in a flowing H_2 atmosphere (high-purity grade, flow rate 0.6 L/min). Two different kinds of heating schedules were used: (i) Constant-heating-rate sintering by heating the green bodies to a pre-set temperature (900-1500 °C) at 5 °C/min without holding, followed by cooling at 10 °C/min down to room temperature. Such experiments were used to investigate sintering kinetics and to search for proper first-step sintering conditions to optimize two-step sintering. (ii) Two-step sintering by firstly heating the green compacts at 5 °C/min to T_1 without holding, then cooling down to T_2 and holding for 10 h, and finally cooling at 10 °C/min down to room temperature.

Powders were inspected under a scanning electron microscope (SEM; Hitachi UHR SU8100) and size distributions were manually measured over 300 particles. Sintered density was measured by the Archimedes method. A theoretical density of 19.25 g/cm^3 [1] was chosen for W to calculate ρ. In constant-heating-rate sintering experiments, sintering rates were calculated from the slopes between each sintering data point and two neighboring data points (or one neighboring data point for the first/last one) in the relative density-time plot. Fractured surfaces of sintered samples were investigated under SEM, with intergranular fracture in all cases. The average grain size G_{avg} and the standard deviation Σ of the measured grain sizes were calculated over 300 measured grains from SEM images. Electron backscatter diffraction (EBSD; using diffractometer HKL Channel 5 on Zeiss Ultra 55 field emission scanning electron microscope) was conducted on polished surfaces (prepared by mechanically polishing followed by electropolishing in NaOH solution). Vickers hardness H was measured on polished surfaces under a load of 200 gf (1.96 N) and with 15 s duration using Vickers diamond pyramid indenter. The distance between neighboring indents was set larger than 500 μm. Weibull modulus m of H was calculated from

$$p(H) = 1 - \exp\left[-(H/H_0)^m\right] \tag{1}$$

Here, H_0 is the characteristic hardness and the probability estimator $p(H)$ is defined as

$$p(H) = (i - 0.3)/(n + 0.4) \tag{2}$$

where i is the rank of the hardness and n=25 is the total number of hardness measurements. This form was chosen to better linearize the skewed Weibull data [30].

3. Results

3.1. Powders

The as-synthesized raw powders of W were inspected under SEM (**Fig. 1a**). Despite the fine average particle size of 69 nm, the raw powders contain many large particles that do not show up in the number-based statistical quantities (e.g., average and median; the latter is known as *D*50). However, as shown by the red data points in **Fig. 1c**, these large particles contribute to much volume fraction, which results in a broad size distribution. The raw powders were sieved to remove most particles above 200 nm and to obtain a narrower size distribution [29] (**Fig. 1b** and **1c**; average particle size of sieved powders is 49 nm). This greatly improves the sinterability in the final stage (ρ>92%) and the effectiveness of two-step sintering, as will be shown later.

3.2. Sintering kinetics from constant-heating-rate experiments

The microstructures of the differently sintered samples in constant-heating-rate experiments (i.e., sintered at a set temperature without holding) were shown in **Fig. 2** and **Supplementary Fig. S1**. The sintered samples using the raw powders show a bimodal-like particle/grain size distribution (**Fig. 2a**) at 900 °C, a non-uniform coarse porous structure (**Fig. 2b**) at 1200 °C, and extensive residual pores (**Fig. 2c**; ρ=95.5% and G_{avg}=1.18 μm) at 1500 °C. In comparison, the ones using the sieved powders show fewer large particles (**Fig. 2d**) at 900 °C, a more uniform and finer porous structure (**Fig. 2e**) at 1200 °C, and a denser microstructure

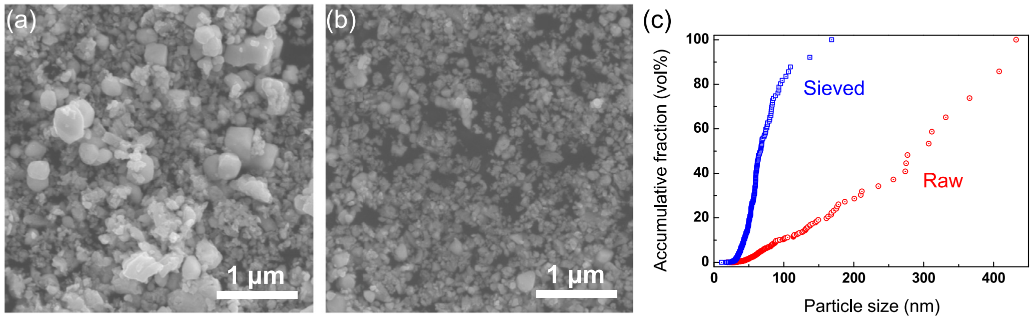

Fig. 1. SEM images of (a) raw and (b) sieved W powders, and (c) their particle size distributions.

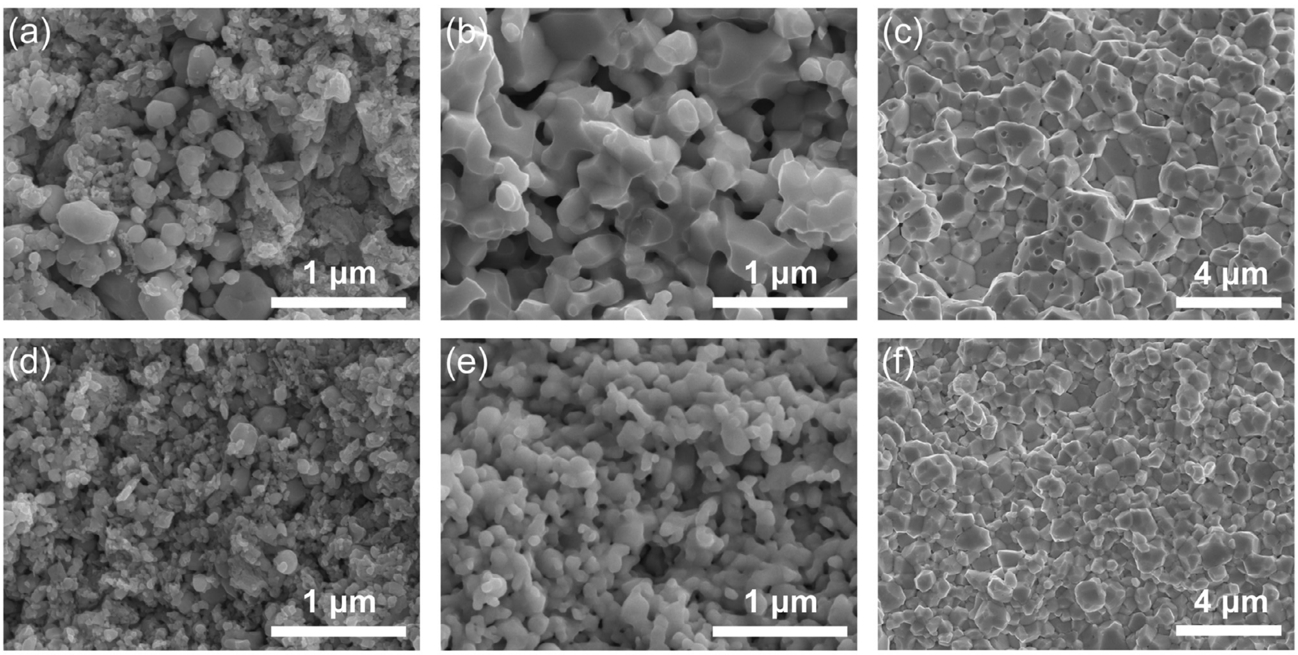

Fig. 2. Microstructures of raw-powder derived samples sintered at (a) 900 °C, (b) 1200 °C, and (c) 1500 °C without holding, and sieved-powder derived samples sintered at (d) 900 °C, (e) 1200 °C, and (f) 1500 °C without holding.

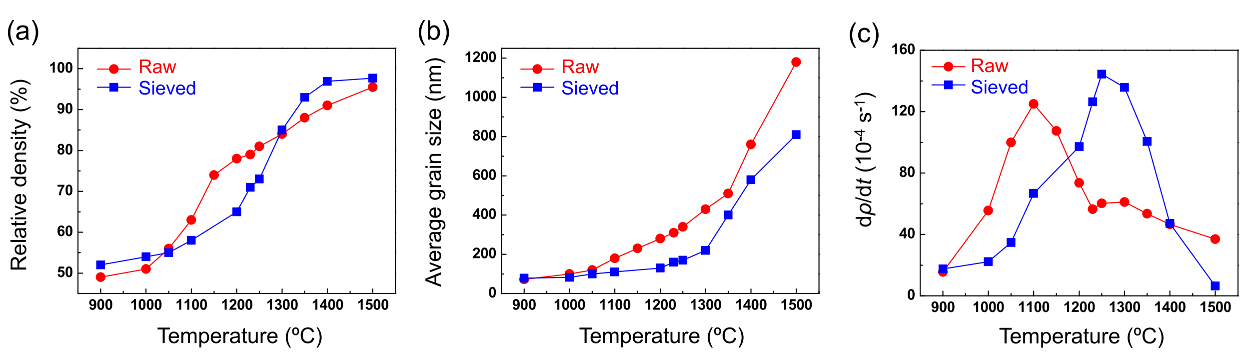

Fig. 3. (a) Relative density ρ, (b) average grain size G_{avg}, and (c) sintering rate $d\rho/dt$ of samples using raw and sieved powders in constant-heating-rate sintering experiments.

(**Fig. 2f**; ρ=97.7% and G_{avg}=0.81 μm) at 1500 °C. The microstructural uniformity, especially the size dispersion, directly affects the sintering kinetics of the two powders (**Fig. 3a** and **3b**). While the sintering of the raw-powder derived samples onsets and reaches the peak rate at lower temperatures than the sieved-powder derived ones, the former becomes exhausted at higher temperatures and densities and is ineffective in further densification in the final sintering stage (ρ higher than ~92%). In comparison, the latter shows a higher peak sintering rate and is able to reach ρ=97.7% at 1500 °C (vs. 95.5% for the former). Interestingly, as shown in **Fig. 3b**, G_{avg} of the former is also consistently higher than that of the latter under the same sintering temperature. These observations suggest that the sintering and grain growth in W have a strong dependence on the size dispersion of the original powders and in compacted samples, where localized sintering and accelerated growth can be triggered by large grains surrounded by finer-size neighbors. It may lead to apparently enhanced sintering at early and intermediate sintering stages, yet on the other hand, bi-

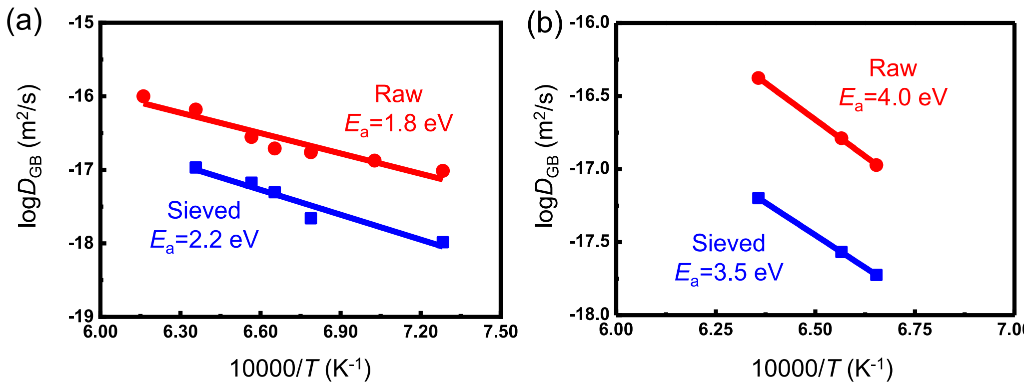

Fig. 4. Arrhenius plot of grain boundary diffusivity D_{GB} calculated by (a) Johnson's method and (b) Herring's method.

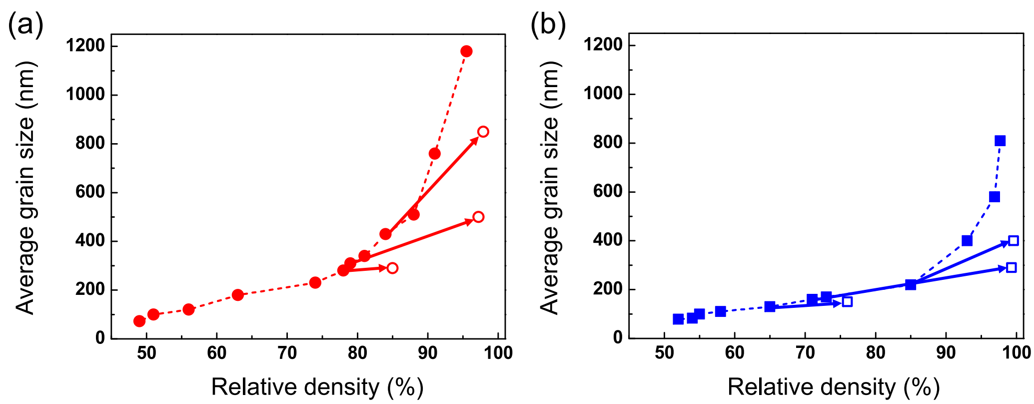

Fig. 5. Grain size-density trajectory of (a) raw-powder and (b) sieved-powder derived samples. Filled symbols denote data from constant-heating-rate sintering without holding and open symbols denote data from two-step sintering. Solid lines with arrows connect the data after the first sintering step to the ones after full two-step sintering schedule. Dash lines are for the guidance of eyes.

furcate the microstructure at a larger length scale, which makes final-stage sintering to 100% density extremely difficult. The sintering rate in **Fig. 3c** and detailed microstructural information allow us to calculate the apparent grain boundary diffusivity D_{GB} and its activation energy E_a from established sintering models. The first one is the sintering model proposed by Johnson [31] (and later adapted by Young and Cutler [32])

$$\left(\frac{\Delta L}{L_0}\right)^{2.06}\frac{d(\Delta L/L_0)}{dt}=\frac{11.2\gamma\Omega\delta D_{GB}}{k_B T G_{avg}^4} \tag{3}$$

where L_0 is the initial sample length, ΔL is the change in length during sintering, $\Delta L/L_0$ is the linear shrinkage, t is the time, γ is the grain boundary energy taken as 2.26 J/m^2 for W [33], Ω is the atomic volume taken as 1.58×10^{-29} m^3, δ is the grain boundary thickness taken as 1 nm, k_B is Boltzmann constant, and T is the absolute temperature in the unit of K. The sintering data above 1100 °C (where major sintering event takes place) and with ρ<90% were analyzed using Johnson's method. The second sintering model is from Herring's general dimensional arguments [34]:

$$\frac{d\rho}{\rho dt}=F(\rho)\frac{3\gamma\Omega\delta D_{GB}}{k_B T G_{avg}^4} \tag{4}$$

where $F(\rho)$ is a dimensionless function depending on ρ and taken as 12,000 for ρ between 0.75 and 0.85 [35]. In both models, E_a can be calculated by assuming an Arrhenius relationship holds for D_{GB}

$$D_{GB}=D_{GB,0}\exp\left(-\frac{E_a}{k_B T}\right) \tag{5}$$

where $D_{GB,0}$ is a constant pre-exponent factor. The obtained D_{GB} and energy E_a from the two models are plotted in **Fig. 4**. In both cases, the sieved-powder derived samples have similar E_a (2.2 eV from Johnson's method and 3.5 eV from Herring's method) to the raw-powder derived ones (1.8 eV from Johnson's method and 4.0 eV from Herring's method). The obtained activation energies here are smaller than the reported ones of pure W in the literature [36–39], which is consistent with the low sintering temperature and implies good sinterability. Meanwhile, D_{GB} is apparently smaller in the sieved-powder derived samples than the raw-powder derived ones, which is consistent with apparently enhanced early-/intermediate-stage sintering for the latter case. This also suggests the inapplicability of the mean-field sintering model to interpret the sintering data of the raw-powder derived samples, where localized sintering and grain growth may dominate. Indeed, while the apparently enhanced D_{GB} gives lower sintering temperature and higher sintering rate for early-/intermediate-stage sintering, its benefit quickly diminished at higher densities, especially the final-stage sintering and ρ>96% cannot be reached even at 1500 °C for the raw-powder derived samples.

3.3. Two-step sintering

As shown by ρ-G_{avg} plot in **Fig. 5**, G_{avg} initially has a linear dependence on ρ, and then accelerated grain growth is triggered at higher ρ (~75% for raw-powder derived samples and ~85% for sieved-powder derived ones). As a result, the second-step sintering at T_2 should start with a lower ρ in order to maximize the benefit of two-step sintering. We thus conducted a systematic search for optimized two-step sintering conditions (**Table 1**). For the raw-powder derived samples, we found ρ=97.9% and G_{avg}=850 nm can be obtained when sintered firstly at T_1=1300 °C for 0 h (i.e., with-

Table 1
Sintering data for constant-heat-rate sintering and two-step sintering under different conditions. Standard deviation Σ of the measured grain sizes are also listed.

Sintering conditions	Raw powders			Sieved powders		
	ρ (%)	G_{avg} (nm)	Σ (nm)	ρ (%)	G_{avg} (nm)	Σ (nm)
900 °C for 0 h	49	72	46	52	79	31
1000 °C for 0 h	51	100	40	54	83	28
1050 °C for 0 h	56	120	50	55	100	30
1100 °C for 0 h	63	180	70	58	110	30
1150 °C for 0 h	74	230	80	/	/	/
1200 °C for 0 h	78	280	90	65	130	40
1230 °C for 0 h	79	310	90	71	160	40
1250 °C for 0 h	81	340	120	73	170	40
1300 °C for 0 h	84	430	150	85	220	60
1350 °C for 0 h	88	510	160	93	400	120
1400 °C for 0 h	91	760	310	96.9	580	230
1500 °C for 0 h	95.5	1180	420	97.7	810	240
1200 °C for 0 h, 1150 °C for 10 h	85	290	100	76	150	40
1230 °C for 0 h, 1150 °C for 10 h	89	320	70	87	200	60
1230 °C for 0 h, 1150 °C for 24 h	96.1	430	120	98.6	340	90
1230 °C for 0 h, 1180 °C for 10 h	97.2	500	180	99.3	290	100
1250 °C for 0 h, 1150 °C for 10 h	91	360	100	90	230	50
1300 °C for 0 h, 1200 °C for 10 h	97.9	850	230	99.6	400	130

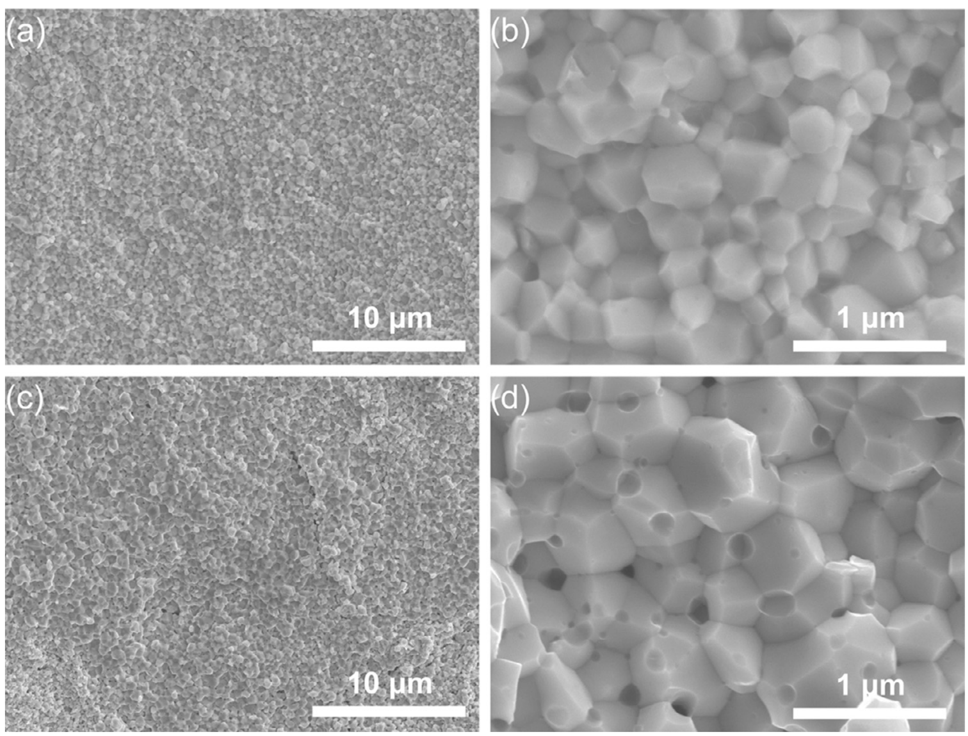

Fig. 6. Fracture surfaces of (a, b) sieved-powder, and (c, d) raw-powder derived samples two-step sintered at T_1=1230 °C for 0 h and then at T_2=1180 °C for 10 h.

out holding) and then at T_2=1200 °C for 10 h, compared to ρ=84% and G_{avg}=430 nm just after the first-step sintering at T_1=1300 °C for 0 h. A lower T_1 results in lower sintered density despite prolonged holding at different T_2, so $\rho\geq$84% is apparently required to start the second-step sintering of the raw-powder derived samples. This is similar to our previous report where $\rho\geq$89% was required to start the second-step sintering and ρ=98.0% and G_{avg}=700 nm were obtained under optimized two-step sintering conditions, despite the different T_1 holding conditions (1 h in our previous report and 0 h in the present work [4]). For the sieved-powder derived samples, we found the second-step sintering can start with ρ as low as 71%. When sintered firstly at T_1=1230 °C for 0 h and then at T_2=1180 °C for 10 h, ρ=99.3% and G_{avg}=290 nm can be obtained, compared to ρ=71% and G_{avg}=160 nm just after the first-step sintering at T_1=1230 °C for 0 h. The resultant fine microstructure shows both low porosity and excellent grain-size uniformity over a large area (Fig. 6**a** and 6**b**), while the raw-powder derived sample sintered under the same condition shows many residual pores (especially at triple grain junctions) and sintering defects (Fig. 6**c** and 6**d**).

For better quantification, EBSD measurements (Fig. 7**a** and 7**e**) were conducted on two-step sintered samples derived from the raw and sieved powders, both sintered at T_1=1230 °C for 0 h and then at T_2=1180 °C for 10 h. The sieved-powder derived sample has not only smaller G_{avg}=293 nm (Fig. 7**b** and 7**f**; similar to G_{avg} measured from SEM images), but also smaller standard deviation Σ=144 nm of grain size G distribution (the standard deviation σ of the normalized grain size distribution G/G_{avg} is similar for both

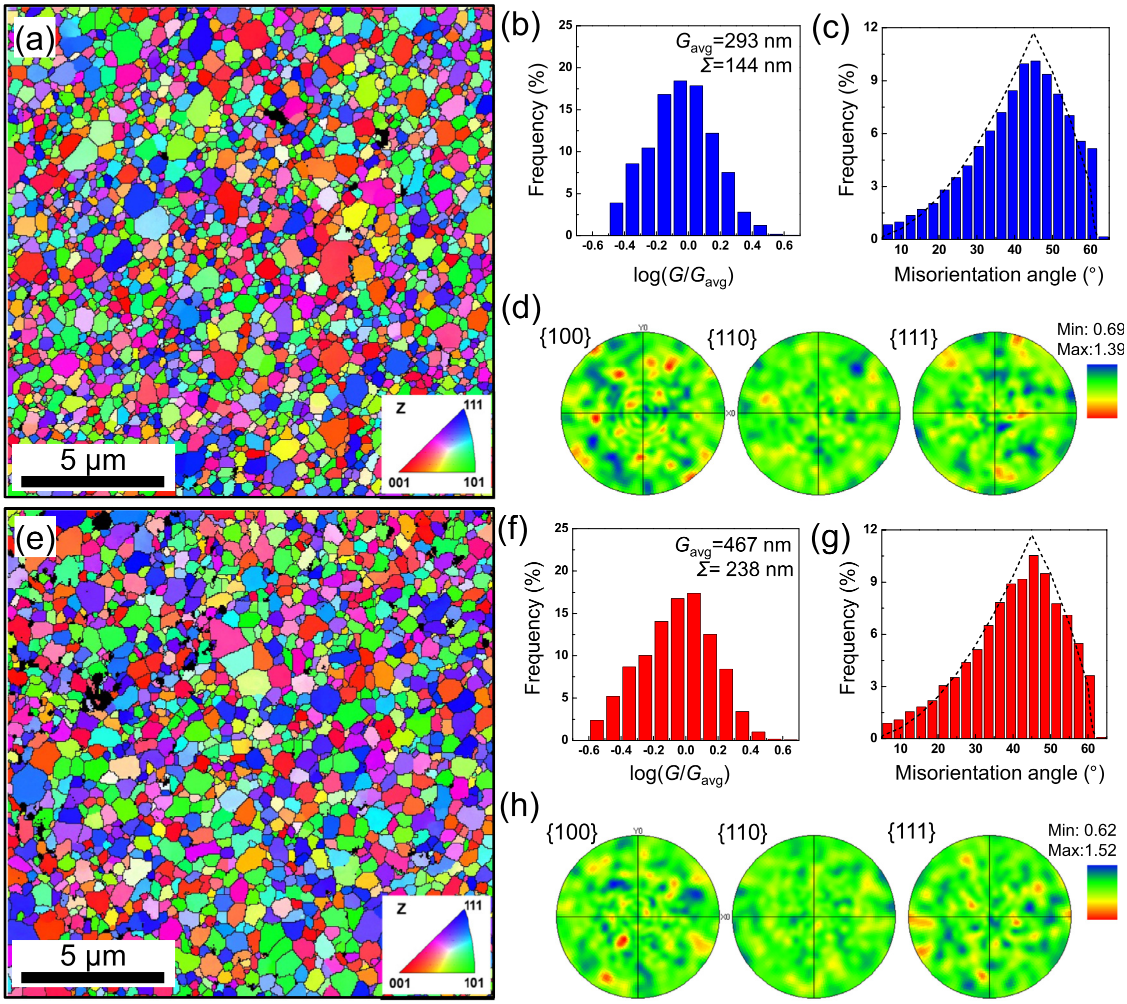

Fig. 7. EBSD results of (a-d) sieved-powder, and (e-h) raw-powder derived samples two-step sintered at T_1=1230 °C for 0 h and then at T_2=1180 °C for 10 h. (a, e) Inverse pole figure map, (b, f) normalized grain size distribution, (c, g) distributions of grain boundary misorientation angles (dash lines: Mackenzie's distribution for randomly oriented cubic grains [40]), and (d, h) pore figures.

samples) than the raw-powder derived one. Σ=144 nm is also much smaller than Σ=300 nm for two-step sintered W reported in Fig. 7b of our previous work [4]. (In our previous work [4], we incorrectly marked Σ by σ in Fig. 7. The correctly marked ones should be Σ=1.00 μm and σ=0.61 in its Fig. 7a, and Σ=0.30 μm and σ=0.39 in its Fig. 7b.) The distributions of grain boundary misorientation angles are similar for both samples (**Fig. 7c** and **7g**), and both agree well with Mackenzie's distribution [40] for randomly oriented cubic grains (dash lines in **Fig. 7c** and **7g**), indicating the absence of preferred orientation and relatively isotropic polycrystal properties. Such isotropy is also evident in the pole figures without obvious texture (**Fig. 7d** and **7h**).

The finer and more uniform microstructure offers better mechanical properties for the sieved-powder derived sample, as demonstrated by the higher hardness H_{avg}=7.8 GPa and the larger Weibull modulus m=30 (**Fig. 8a**), compared to H_{avg}=5.8 GPa and m=13 for the raw-powder derived one. The hardness data are plotted against $G_{avg}{}^{-1/2}$ in **Fig. 8b** and compared with literature reports [4,15,16,41,42], which represent the finest G_{avg} and highest H_{avg} among all pressureless sintering data of pure W. Meanwhile, the Hall-Petch relationship holds, indicating good grain boundary cohesion without apparent softening. This indicates the elimination of T_1 holding would not introduce much oxygen impurity that harms mechanical properties.

4. Discussions

In addition to the technological advance in producing pressureless sintered ultrafine-grained W (G_{avg}=290 nm) close to full density (ρ=99.3%) and towards nano-crystallinity, we can now answer the four opening questions imposed in the Introduction section. For question (1), full density and good grain boundary cohesion can be reached without T_1 holding, so it is not a necessity. By eliminating T_1 holding, we do not observe any effect of oxygen impurity in sintering or hardness. For question (2), ρ_c≈71% is sufficiently high to start the second-step sintering for W. This initial value for the T_2 step is comparable to that for isotropic ceramic systems including $BaTiO_3$ [20], Y_2O_3 [18,19], and $Ni_{0.2}Cu_{0.2}Zn_{0.6}Fe_2O_4$ [20], and much smaller than that for Al_2O_3 which is rather anisotropic [21,22]. For question (3), a minimum T_2=1180 °C is found to be necessary for full densification in 10 h, increasing ρ=71% and G_{avg}=160 nm to ρ=99.3% and G_{avg}=290 nm, respectively. A lower T_2=1150 °C leads to much slower densification, increasing ρ=71% and G_{avg}=160 nm to ρ=87% and G_{avg}=200 nm in 10 h, and to ρ=98.6% and G_{avg}=340 nm in 24 h, respectively. It shows that a 1.8-fold grain size coarsening still takes place in optimized two-step sintering of W, and a constant-grain-size second-step sintering has not been achieved, which is different from many ceramic systems including $BaTiO_3$ [20], Y_2O_3

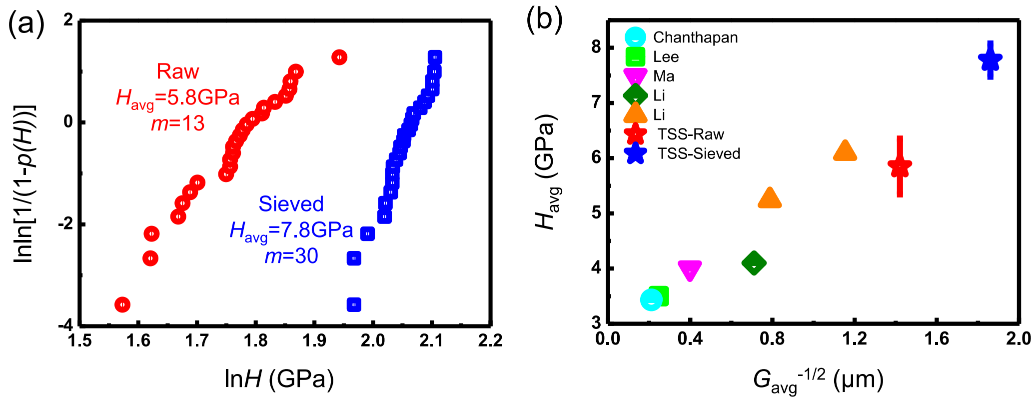

Fig. 8. (a) Weibull distribution of measured Vickers hardness for two-step sintered W at T_1=1230 °C for 0 h and then at T_2=1180 °C for 10 h. (b) Comparison of hardness data with the literature reports [4,15,16,41,42].

[18,19], $Ni_{0.2}Cu_{0.2}Zn_{0.6}Fe_2O_4$ [20], and Al_2O_3 [21,22]. This may be attributed to the difference between oxides and powder metallurgy. For question (4), the two-step sintered W gives G_{avg}=290 nm at minimum. 6-fold coarsening from the average particle size of the initial powders is realized, among which 3-fold takes place in the first-step sintering and 2-fold in the second-step sintering. The former is comparable to that in the best practiced ceramic system (2 for $BaTiO_3$-based ceramics [20] and 6-10 for Al_2O_3 [21,22], both contributing by the first-step sintering only).

Our work further highlights the critical role of the initial powders in practicing and optimizing two-step sintering, where T_1, T_2, ρ_c, G_{avg} can be simultaneously decreased and the density, uniformity, properties and reliability of the sintered samples can be much improved. It should be mentioned that while the sieving process works relatively well, it cannot completely remove the large particles. We suspect that it is due to the formation of hard agglomerations, where particles are chemically bonded and cannot be effectively separated by mechanical grinding, stirring, or ultrasonic treatment. This is a major issue to be addressed in the future.

Comparing the two-step sintering of metallic W with ceramics, many similarities are noted, and a $\rho_c\approx$71% is especially appreciated. The latter indicates a low anisotropy in interfacial energy distribution of W, so that shrinking the pores with the least favorable dihedral angles is not too difficult. However, we also note relatively fast grain growth kinetics in W, which cannot be completely frozen even at T_2=1180 °C, which is only about 0.39 of its melting temperature (3695 K for W). In comparison, T_2=1025 °C is sufficient to completely freeze grain growth in the second-step sintering of Al_2O_3 with G_{avg}=34 nm [3], which is about 0.55 of the melting temperature of Al_2O_3 (2345 K). It indicates more active grain growth kinetics in W than in Al_2O_3 at the same homologous temperature (T/T_m), showing the difference between oxides and an elemental metal. It may be related to smaller Burgers vectors in metallic systems, which makes shear-coupled grain boundary migration [43] relatively easier at relatively low temperatures.

Lastly, regarding the future research to achieve pressureless sintering of nanocrystalline W, we believe the key lies in optimized nanopowders with ultralow powder size dispersity and also the forming technique to prepare better green bodies. Since a coarsening factor of 6 from powders to sintered samples can be realized, high-purity nanopowders with 15-20 nm particle size should be developed, and hard agglomerations should at least be minimized if not completely eliminated. Meanwhile, warm pressing, warm isostatic pressing, and colloidal processing techniques should be investigated to improve the compact density and uniformity of the green body. The combined efforts are promising to further refine the pressureless sintered W as well as other refractory metals and alloys with better properties and reliability.

5. Conclusions

(1) Pressureless two-step sintering of W has been further developed by sieving away large particles/agglomerates in the initial powders and optimizing processing conditions. It offers ultrafine grain size (290 nm) and a uniform microstructure for high-density W (ρ>99%), without any observable texture or abnormal grains.

(2) Hardness is improved due to finer and more uniform microstructure. The Hall-Petch relationship holds for pressureless sintered W, down to 290 nm and a hardness of 7.8 GPa.

(3) T_1 holding is not necessary for successful two-step sintering of W. Eliminating T_1 holding preserves sinterability and good grain boundary cohesion.

(4) Benefiting from the sieved powders, a low $\rho_c\approx$71%, comparable to the smallest values in isotropic ceramic systems (e.g., $BaTiO_3$, Y_2O_3 and $Ni_{0.2}Cu_{0.2}Zn_{0.6}Fe_2O_4$), is found sufficient to start the second-step sintering of W. A minimum T_2=1180 °C, or 0.39 of the melting point, is found sufficient for the second-step sintering for full densification within reasonable heat-treatment time (e.g., 10 h in flowing H_2). Grain growth is still active at this temperature.

(5) 6-fold coarsening is realized from the average particle size of the initial powders to the average grain size of the fully dense sample. It includes 3-fold coarsening in the first-step sintering, which is similar to the best practice in oxide systems, and another 2-fold coarsening in the second-step sintering, which can be completely absent in some oxide ceramics.

(6) The lessons learned offer scientific understanding and technological guidance towards pressureless sintering of bulk nanocrystalline W and other refractory metals and alloys.

Declaration of Competing Interest

The authors declare that they have no known competing financial interests or personal relationships that could have appeared to influence the work reported in this paper.

Acknowledgment

X.L., L.Z., M.Q., Z.W., Z.Q., J.Y., and X.Q. acknowledge the financial supports by National Key R&D Program of China (2017YFB0305600), Natural Science Foundation of China (52074032, 51974029, 52071013, 5213000708) and 111 Project (No. B170003). Y.D. and J.L. acknowledge the support by Eni S.p.A. through the MIT Energy Initiative.

Supplementary materials

Supplementary material associated with this article can be found, in the online version, at doi:10.1016/j.actamat.2021.117344.

References

[1] E. Lassner, W.D. Schubert, Tungsten: Properties, Chemistry, Technology of the Element, Alloys and Chemical Compounds, Kluwer Academic and Plenum Publishers, New York, 1999.
[2] W.F. Smith, Structure and Properties of Engineering Alloys, 2nd ed., New York, 1993.
[3] Y. Dong, H. Yang, L. Zhang, X. Li, D. Ding, X. Wang, J. Li, J. Li, I. Chen, Ultra-Uniform Nanocrystalline Materials via Two-Step Sintering, Adv. Funct. Mater. 31 (2021) 2007750.
[4] X. Li, L. Zhang, Y. Dong, R. Gao, M. Qin, X. Qu, J. Li, Pressureless two-step sintering of ultrafine-grained tungsten, Acta Mater 186 (2020) 116–123.
[5] P. Zhao, H. Wang, L. Wu, L. Chen, Z. Cai, L. Li, X. Wang, High-Performance Relaxor Ferroelectric Materials for Energy Storage Applications, Adv. Energy Mater. 9 (2019) 1803048.
[6] C. Linsmeier, M. Rieth, J. Aktaa, T. Chikada, A. Hoffmann, J. Hoffmann, A. Houben, H. Kurishita, X. Jin, M. Li, A. Litnovsky, S. Matsuo, A. von Müller, V. Nikolic, T. Palacios, R. Pippan, D. Qu, J. Reiser, J. Riesch, T. Shikama, R. Stieglitz, T. Weber, S. Wurster, J.-H. You, Z. Zhou, Development of advanced high heat flux and plasma-facing materials, Nucl. Fusion. 57 (2017) 092007.
[7] H.W. Hayden, J.H. Brophy, The Activated Sintering of Tungsten with Group VIII Elements, J. Electrochem. Soc. 110 (1963) 805.
[8] M. Park, C.A. Schuh, Accelerated sintering in phase-separating nanostructured alloys, Nat. Commun. 6 (2015) 6858.
[9] T. Chookajorn, H.A. Murdoch, C.A. Schuh, Design of Stable Nanocrystalline Alloys, Science 337 (2012) 951–954.
[10] J.L. Johnson, Activated liquid phase sintering of W-Cu and Mo-Cu, Int. J. Refract. Met. Hard Mater. 53 (2015) 80–86.
[11] V.K. Gupta, D. Yoon, H.M. Meyer, J. Luo, Thin intergranular films and solid-state activated sintering in nickel-doped tungsten, Acta Mater 55 (2007) 3131–3142.
[12] G. Prabhu, A. Chakraborty, B. Sarma, Microwave sintering of tungsten, Int. J. Refract. Met. Hard Mater. 27 (2009) 545–548.
[13] M.A. Monge, M.A. Auger, T. Leguey, Y. Ortega, L. Bolzoni, E. Gordo, R. Pareja, Characterization of novel W alloys produced by HIP, J. Nucl. Mater. 386–388 (2009) 613–617.
[14] P. Liu, F. Peng, F. Liu, H. Wang, C. Xu, Q. Wang, X. Zhou, W. Yin, S. Yin, Y. Li, D. He, High-pressure preparation of bulk tungsten material with near-full densification and high fracture toughness, Int. J. Refract. Met. Hard Mater. 42 (2014) 47–50.
[15] S. Chanthapan, A. Kulkarni, J. Singh, C. Haines, D. Kapoor, Sintering of tungsten powder with and without tungsten carbide additive by field assisted sintering technology, Int. J. Refract. Met. Hard Mater. 31 (2012) 114–120.
[16] J. Ma, J. Zhang, W. Liu, Z. Shen, Suppressing pore-boundary separation during spark plasma sintering of tungsten, J. Nucl. Mater. 438 (2013) 199–203.
[17] S. Deng, R. Li, T. Yuan, S. Xie, M. Zhang, K. Zhou, P. Cao, Direct current-enhanced densification kinetics during spark plasma sintering of tungsten powder, Scr. Mater. 143 (2018) 25–29.
[18] I.-W. Chen, X.-H. Wang, Sintering dense nanocrystalline ceramics without final-stage grain growth, Nature 404 (2000) 168–171.
[19] X. Wang, P. Chen, I. Chen, Two-Step Sintering of Ceramics with Constant Grain–Size, I. Y_2O_3, J. Am. Ceram. Soc. 89 (2006) 431–437.
[20] X. Wang, X. Deng, H. Bai, H. Zhou, W. Qu, L. Li, I. Chen, Two-Step Sintering of Ceramics with Constant Grain-Size, II: $BaTiO_3$ and Ni-Cu-Zn Ferrite, J. Am. Ceram. Soc. 89 (2006) 438–443.
[21] H. Yang, L. Li, W. Cao, Y. Liu, M. Mukhtar, L. Zhao, Y. Kang, Y. Dong, J. Li, Sintering kinetics and microstructure evolution in α-Al_2O_3 nanocrystalline ceramics: Insensitive to Fe impurity, J. Eur. Ceram. Soc. 40 (2020) 1505–1512.
[22] H. Yang, L. Li, Y. Li, B. Shen, Y. Kang, L. Zhao, J. Li, Y. Dong, J. Li, Unveiling exceptional sinterability of ultrafine α-Al_2O_3 nanopowders, J. Materiomics 7 (2021) 837–844.
[23] Y. Dong, I. Chen, Mobility transition at grain boundaries in two-step sintered 8 mol% yttria-stabilized zirconia, J. Am. Ceram. Soc. 101 (2018) 1857–1869.
[24] M. Mazaheri, M. Valefi, Z.R. Hesabi, S.K. Sadrnezhaad, Two-step sintering of nanocrystalline $8Y_2O_3$ stabilized ZrO_2 synthesized by glycine nitrate process, Ceram. Int. 35 (2009) 13–20.
[25] M. Mazaheri, A.M. Zahedi, S.K. Sadrnezhaad, Two-Step Sintering of Nanocrystalline ZnO Compacts: Effect of Temperature on Densification and Grain Growth, J. Am. Ceram. Soc. 91 (2010) 56–63.
[26] M. Mazaheri, Z. Razavi Hesabi, S.K. Sadrnezhaad, Two-step sintering of titania nanoceramics assisted by anatase-to-rutile phase transformation, Scr. Mater. 59 (2008) 139–142.
[27] A. Polotai, K. Breece, E. Dickey, C. Randall, A. Ragulya, A Novel Approach to Sintering Nanocrystalline Barium Titanate Ceramics, J. Am. Ceram. Soc. 88 (2010) 3008–3012.
[28] M. Qin, Z. Chen, P. Chen, S. Zhao, R. Li, J. Ma, X. Qu, Fabrication of tungsten nanopowder by combustion-based method, Int. J. Refract. Met. Hard Mater. 68 (2017) 145–150.
[29] E.A. Barringer, H.K. Bowen, Ceramic Powder Processing, in: Ceram. Eng. Sci. Proc. (2008) 285–297.
[30] B. Bergman, On the estimation of the Weibull modulus, J. Mater. Sci. Lett. 3 (1984) 689–692.
[31] D.L. Johnson, New method of obtaining volume, grain-boundary, and surface diffusion coefficients from sintering data, J. Appl. Phys. 40 (1969) 192–200.
[32] W.S. Young, I.B. Cutler, Initial Sintering with Constant Rates of Heating, J. Am. Ceram. Soc. 53 (1970) 659–663.
[33] D. Scheiber, R. Pippan, P. Puschnig, L. Romaner, Ab initio calculations of grain boundaries in bcc metals, Model. Simul. Mater. Sci. Eng. 24 (2016) 035013.
[34] C. Herring, Effect of change of scale on sintering phenomena, J. Appl. Phys. 21 (1950) 301–303.
[35] J.D. Hansen, R.P. Rusin, M. Teng, D.L. Johnson, Combined-Stage Sintering Model, J. Am. Ceram. Soc 75 (1992) 1129–1135.
[36] N.C. Kothari, Sintering kinetics in tungsten powder, J. Less-Common Met. 5 (1963) 140–150.
[37] T. Vasilos, J.T. Smith, Diffusion mechanism for tungsten sintering kinetics, J. Appl. Phys. 35 (1964) 215–217.
[38] R.M. German, Z.A. Munir, Enhanced low-temperature sintering of tungsten, Metall. Trans. A. 7 (1976) 1873–1877.
[39] A.K. Srivastav, M. Sankaranarayana, B.S. Murty, Initial-stage sintering kinetics of nanocrystalline tungsten, Metall. Mater. Trans. A Phys. Metall. Mater. Sci. 42 (2011) 3863–3866.
[40] J.K. Mackenzie, Second Paper on Statistics Associated with the Random Disorientation of Cubes, Biometrika 45 (1958) 229.
[41] B. Li, Z. Sun, G. Hou, F. Ding, P. Hu, F. Yuan, The sintering behavior of quasi-spherical tungsten nanopowders, Int. J. Refract. Met. Hard Mater. 56 (2016) 44–50.
[42] G. Lee, J. McKittrick, E. Ivanov, E.A. Olevsky, Densification mechanism and mechanical properties of tungsten powder consolidated by spark plasma sintering, Int. J. Refract. Met. Hard Mater. 61 (2016) 22–29.
[43] J. Han, S.L. Thomas, D.J. Srolovitz, Grain-boundary kinetics: A unified approach, Prog. Mater. Sci. 98 (2018) 386–476.